

Summer precipitation variability over South America on long and short intraseasonal timescales

Article

Accepted Version

Gonzalez, P. L. M. ORCID: <https://orcid.org/0000-0003-0154-0087> and Vera, C. S. (2014) Summer precipitation variability over South America on long and short intraseasonal timescales. *Climate Dynamics*, 43 (7). pp. 1993-2007. ISSN 0930-7575 doi: <https://doi.org/10.1007/s00382-013-2023-2> Available at <https://centaur.reading.ac.uk/85688/>

It is advisable to refer to the publisher's version if you intend to cite from the work. See [Guidance on citing](#).

To link to this article DOI: <http://dx.doi.org/10.1007/s00382-013-2023-2>

Publisher: Springer

All outputs in CentAUR are protected by Intellectual Property Rights law, including copyright law. Copyright and IPR is retained by the creators or other copyright holders. Terms and conditions for use of this material are defined in the [End User Agreement](#).

www.reading.ac.uk/centaur

CentAUR

Central Archive at the University of Reading

Reading's research outputs online

1 **Summer precipitation variability over South America on long**
2 **and short intraseasonal timescales**

3
4 **Paula L. M. Gonzalez ¹, Carolina S. Vera ²**

5
6 **1.** International Research Institute for Climate and Society, Columbia University

7 61 Route 9W, 202b Monell, Palisades, NY 10964 USA

8 Tel.: +1-845-6804525 / Fax: +1-845-6804865

9 E-mail: gonzalez@iri.columbia.edu

10
11 **2.** Centro de Investigaciones del Mar y la Atmosfera (CIMA/CONICET-UBA), DCAO/FCEN, UMI
12 IFAECI/CNRS

13 2^{do} piso, Pabellon II, Ciudad Universitaria, 1428, Buenos Aires, Argentina.

14 Tel.: +54-11-4787-2693/ Fax: +54-11-4788-3592

15 E-mail: carolina@cima.fcen.uba.ar

16
17
18 **ABSTRACT**

19 A dipole pattern in convection between the South Atlantic Convergence Zone and the subtropical
20 plains of southeastern South America characterizes summer intraseasonal variability over the
21 region. The dipole pattern presents two main bands of temporal variability, with periods between
22 10 and 30 days, and 30 and 90 days; each influenced by different large-scale dynamical forcings.
23 The dipole activity on the 30-90-day band is related to an eastward traveling wavenumber-1
24 structure in both OLR and circulation anomalies in the tropics, similar to that associated with the
25 Madden-Julian Oscillation. The dipole is also related to a teleconnection pattern extended along
26 the South Pacific between Australia and South America. Conversely, the dipole activity on the 10-
27 30-day band does not seem to be associated with tropical convection anomalies. The

28 corresponding circulation anomalies exhibit, in the extratropics, the structure of Rossby-like wave
29 trains, although their sources are not completely clear.

30 **Keywords** summer precipitation, intraseasonal variability, South America, SASS, MJO

31 **1. Introduction**

32

33 The most distinctive feature of summer rainfall variability on intraseasonal timescales over
34 South America (SA) is a dipolar pattern known as South American Seesaw (SASS) (e.g.; Casarin and
35 Kousky 1986; Nogues-Paegle and Mo 1997; Diaz and Aceituno 2003). SASS exhibits centers of
36 action of opposite sign in both the South Atlantic convergence zone (SACZ) and southeastern
37 South America (SESA) regions. The phase with enhanced precipitation over the subtropics and a
38 weak SACZ – hereafter ‘positive phase’ - is associated with increased southward moisture flux
39 from the Amazon region to SESA, favored by the presence of a low-level jet to the east of the
40 Andes (Nogues-Paegle and Mo 1997). In the opposite phase, a SACZ enhancement is accompanied
41 by increased southeast moisture fluxes from the Amazon region to SACZ and decreased rainfall at
42 the subtropical plains – hereafter ‘negative phase’. It has been shown that in both phases, the
43 region with enhanced precipitation is more likely to experience extreme rainfall events (e.g.;
44 Carvalho et al. 2004; Liebmann et al. 2004; Gonzalez et al. 2008). Furthermore, Cerne et al. (2007)
45 and Cerne and Vera (2011) showed that during the phase of enhanced SACZ (negative phase of
46 SASS), the associated subsidence promotes a larger frequency of heat waves and extreme heat
47 events over the subtropical center, evidencing that SASS influence is not only restricted to
48 convection and precipitation.

49 Previous works suggest that SASS is not only a regional feature but also part of a large-
50 scale system (e.g.; Nogues-Paegle and Mo 1997). In particular, Kalnay et al. (1986) and Grimm and
51 Silva Dias (1995) first detected interactions between the SACZ and the South Pacific convergence
52 zone (SPCZ, Vincent 1994) on intraseasonal timescales. Subsequent studies have suggested that
53 the development of Rossby wave trains, forced by the tropical convective activity of the Madden-
54 Julian Oscillation (MJO), influences intraseasonal variability over SA. This interaction between
55 tropics and extratropics is frequently linked to the development of Pacific-South America (PSA)
56 teleconnection patterns (e.g.; Mo and Higgins 1998), as is also observed on interannual timescales

57 (e.g.; Mo and Nogues-Paegle 2001). Li and Le Treut (1999) showed that in winter as well as in
58 summer, a certain phase of the PSA patterns on intraseasonal timescales may induce changes in
59 the moisture transport channeled by the Andes from the Amazon region towards SESA. In
60 addition, Cunningham and Cavalcanti (2006) identified two modes of intraseasonal variability
61 affecting the SACZ, both with timescales between 30 and 60 days. The first mode represents the
62 tropics-tropics interactions and is characterized by a northward displacement of the SACZ with
63 respect to its climatological position. The second mode is related to the tropics-extratropics
64 interactions and is associated with PSA-like patterns.

65 Nonetheless, SASS activity is not only restricted to the 30-60 day band. Liebmann et al.
66 (1999) showed that OLR intraseasonal variability over the SACZ and the Amazon basin exhibits the
67 most relevant spectral peaks at approximately 48, 27, and 16 days. Consistently, through a singular
68 spectrum analysis, Nogues-Paegle et al. (2000) isolated two main oscillatory modes associated
69 with the SASS Index: one mode with longer periods of variability, between 36 and 40 days (*mode*
70 *40*); and the other mode with shorter periods, between 22 and 28 days (*mode 20*). OLR anomalies
71 related to mode 20 seem to be more relevant over SESA than those associated with mode 40,
72 while both modes interfere constructively in the negative phase of SASS (Nogues-Paegle et al.
73 2000). While mode 40 variability has been linked to MJO activity, the sources of that associated
74 with mode 20 remain unclear.

75 The existent bibliography reveals a special interest on the study of the influence of MJO on
76 South American climate, mainly motivated by the fact that MJO is the only intraseasonal
77 oscillation with a demonstrated degree of predictability (e.g.; Ferranti et al. 1990; Waliser et al.
78 2003). Nevertheless, different studies have shown that state-of-the-art CGCMs are still deficient at
79 representing the MJO activity (e.g.; Slingo et al. 1996) and consequently its influence on
80 precipitation over SA (e.g.; Lin et al. 2006). Consequently, a profound understanding of such
81 influence together with an improvement in its representation in GCMs could potentially extend
82 the predictability of summer precipitation over SA (Nogues-Paegle et al. 1997; Jones and Schemm
83 2000; Cavalcanti and Castro 2003; Cunningham and Cavalcanti 2006). In addition, since MJO only
84 explains a small percentage of intraseasonal variability in both subtropical and tropical regions, a
85 more profound understanding of other sources of such variability over SA is also needed.

86 The objective of this paper is to further explore the physical mechanisms that explain SASS
87 activity on both short (10-30 days) and long (30-90 days) intraseasonal time scales. The work

88 focuses on better understanding the remote forcings of variability in each activity band separately,
89 and to assess whether they act through different dynamical mechanisms. In turn, these results
90 could be useful to identify the strengths and weaknesses of the representation of intraseasonal
91 variability in state-of-the-art general circulation models and to exploit the potential predictability
92 of these processes.

93

94 **2. Data and methodology**

95

96 The NOAA interpolated OLR dataset (Liebmann and Smith 1996) over the 1979-2007
97 period (28 warm seasons) was considered to describe intraseasonal variability of convection over
98 SA. The warm season was represented by the November-March (151 days) period. Filtered OLR
99 (FOLR) anomalies were calculated through a Lanczos band-pass filter (Duchon 1979) for both
100 bands: 10-30 days (hereafter FOLR 10-30) and 30-90 days (hereafter FOLR 30-90).

101 The leading patterns of variability were isolated for both activity bands, performing two
102 separate Empirical Orthogonal Functions (EOF) analyses of the corresponding FOLR anomalies over
103 SA. In both cases, as it is discussed in the next section, the leading patterns resemble the spatial
104 features associated with SASS. The corresponding standardized principal component time series
105 are considered as the SASS indexes. It is worth mentioning that the methodology used in this work
106 to isolate the leading patterns for the two temporal bands is different from that used in previous
107 studies. For example, Nogues-Paegle et al. (2000) performed first an EOF analysis of the FOLR
108 anomalies representing the full range of intraseasonal timescales (10-90 days) and then they
109 discriminated the SASS signal in both intraseasonal bands through a singular spectrum analysis. In
110 this work we chose to isolate first the FOLR anomalies associated with each temporal band, and
111 then performed the EOF analyses to identify the corresponding SASS patterns (hereafter called
112 SASS 10-30 and SASS 30-90, respectively). This approach was motivated by several points: the fact
113 that MJO concentrates its activity on the 30-90 day band; the previous works that showed the
114 relevance of SASS in both variability bands; and the limitations of an EOF analysis performed in S-
115 mode (which is the usual way of applying EOF), which might not be an appropriate tool to

116 discriminate variability patterns with different dominant timescales (e.g.; Bjornsson and Venegas
117 1997).

118 Lagged daily regression maps of FOLR fields were computed using the SASS indexes as
119 reference time series. Lagged regression maps were also constructed for streamfunction zonal
120 anomalies at sigma level $\sigma = 0.2101$, available from NCEP/NCAR Reanalysis (Kalnay et al. 1996).
121 Statistically significant regression values were identified through a two-tailed Student t-test of the
122 corresponding correlation values at a significance level of 0.05.

123

124 **3. SASS Dynamics**

125 The SASS patterns obtained through the EOF analysis of both FOLR 30-90 and FOLR 10-30
126 anomalies are displayed in Figure 1. The SASS 30-90 explains 21.8 % of the variance and exhibits
127 two centers of action over the SACZ and SESA regions, as identified in previous works. The loadings
128 are much larger over the SACZ region than over SESA, and both centers exhibit a strong NW-SE
129 orientation (Fig. 1a). On the other hand, the SASS 10-30 explains 14 % of the variance and it also
130 exhibits a dipole-like structure, with loadings over SACZ slightly larger than those over SESA (Fig.
131 1b). A comparison of the amplitude of the two SASS patterns shows that the two centers of SASS
132 10-30 are stronger than the corresponding ones of SASS 30-90. In addition, in the case of SASS 30-
133 90, the NW-SE tilt seems to be somewhat weaker, particularly in the SACZ center.

134 The spectral properties of both SASS patterns obtained from the corresponding SASS
135 indexes are presented in Figure 2. SASS 10-90 exhibits 3 significant activity peaks at around 44, 57
136 and 35 days. On the other hand, the SASS 10-30 presents peaks at around 15 and 23 days .

137

138 **3.1 SASS 30-90**

139

140 The large-scale FOLR 10-90 anomalies related to SASS 30-90 activity are described using
141 regression maps between lags -30 and +30 days (Figure 3). A negative day implies that FOLR
142 anomalies temporarily lead the SASS 30-90 index. Between days -30 and -20, FOLR anomalies over

143 SA suggest the development of the SACZ, with an expansion of convection towards the equatorial
144 Atlantic. During that time, the Pacific Ocean is characterized by a suppressed SPCZ and inhibited
145 convection over the warm pool. By day -25, the development of a dipolar structure is discernible
146 over SA, consistent with a negative phase of SASS. Inhibited convection over the Maritime
147 Continent (MC) and increased convection over Africa are also evident; a structure that exhibits
148 eastward propagation during the following days. Between days -20 and -15, the dipolar structure
149 over SA weakens and by day -10 a positive phase of SASS starts to develop, and peaks on day 0. In
150 agreement, convection over both SACZ and Africa weakens, while it intensifies over the western
151 portion of tropical South Pacific with a NW-SE orientation, consistent with a strengthened SPCZ.
152 Between days 0 and +10, the positive phase of SASS weakens, while enhanced (weakened)
153 convection over the MC-western tropical Pacific (Africa-tropical Indian sector) continues its
154 eastward propagation. In addition, from day +5 onwards, the SPCZ evolves towards an inhibited
155 phase. Between days +10 and +15, SASS transitions to a negative phase. On day +20 the SACZ
156 intensifies, and so does convection over southern Africa, with a NW-SE orientation that could be
157 associated with the so called South Indian convergence zone (SICZ, e.g.; Cook 2000), but shifted to
158 the SW. This SICZ behavior has been identified as an evidence of the interaction between
159 convection in SA and Africa (Cook et al. 2004).

160 The SASS 30-90 evolution is similar to that described by Nogues-Paegle et al. (2000) for
161 their mode 40. It is also highly consistent at the tropical band with the MJO life cycle (e.g.; Hendon
162 and Salby 1994), characterized by a zonally oriented convection dipole that propagates eastward
163 along the Equator, from the Indian Ocean to the central Pacific. As it has been described before,
164 such convective anomalies tend to dissipate as they approach the eastern Pacific, where sea
165 surface temperatures (SST) become colder. Consistently, the analyzed regression maps do not
166 show any significant eastward propagation of convection anomalies over tropical SA in association
167 with SASS 30-90 evolution. The fact that SASS remains stationary seems to be related to the SACZ,
168 which is anchored to the continent by the convection associated with the South American
169 Monsoon System (e.g.; Kalnay et al. 1986). The study of the lag-by-day regression time series for
170 two grid points located at each SASS dipole centers (Fig. 4) reveals that the evolution of both
171 centers is highly antisymmetrical, completing a full cycle in approximately 40 days.

172 The large-scale circulation anomalies associated with the SASS 30-90 evolution are
173 described through the analysis of the regression maps of upper-level streamfunction anomalies

174 (Fig. 5). Zonal means have been removed from the regressed values in order to highlight the zonal
175 assymetries. The regression maps reveal a wavenumber-1 structure in circulation anomalies at the
176 tropical band that propagates eastward during the whole evolution, resembling that observed in
177 the MJO life cycle. In particular, tropical circulation anomalies persist across the dateline,
178 explaining the connection between convection anomalies in the Indian and western Pacific oceans
179 with those over tropical America (Fig. 3). Figure 6 presents the Hovmöller diagrams of
180 streamfunction regressed anomalies along the tropical band. Eastward propagation of the
181 anomalies is clear between the Indian Ocean and southeastern Pacific, while they acquire a more
182 stationary character over SA.

183 Regression maps also show circulation anomalies organized in wave trains extended along
184 the South Pacific Ocean, and reaching mid- and high-latitudes (Fig. 5). A clear example can be seen
185 between days -15 and day 0, when opposite sign centers alternate from the Indian and western
186 Pacific oceans towards the high latitudes of the Southern Hemisphere, along an arch-shaped
187 trajectory that reaches SA. The development of such wavetrain occurs while tropical convection
188 intensifies over the MC-western equatorial Pacific sector (Fig. 3). As it was mentioned before,
189 these teleconnection patterns are consistent with those described by Nogues-Paegle et al. (2000)
190 for their mode 40 and they are linked to meridionally propagating Rossby waves (Sardeshmukh
191 and Hoskins 1988). They have been identified in the Southern Hemisphere as the PSA patterns,
192 and can be modulated by tropical convection (e.g.; Mo and Higgins 1998; Mo and Nogues-Paegle
193 2001). In addition, between approximately day -15 and day +5, a quasistationary wavenumber 3
194 pattern is discernible at high latitudes. In agreement, Mo and Higgins (1998) found that the two
195 leading patterns of circulation anomalies in the South Pacific on intraseasonal timescales resemble
196 PSA-like structure and are in quadrature by each other, with a signature of wavenumber 3 at
197 midlatitudes.

198 On day 0, it is evident that in association with a SASS 30-90 positive phase the
199 extratropical teleconnection pattern induces cyclonic (anticyclonic) anomalies at extratropical
200 (tropical) SA. That regional circulation anomaly pattern is consistent with wetter than normal
201 conditions in SESA and dryer conditions in the SACZ region. Between days -5 and +5, another arch-
202 shaped wave train structure is evident across the South Atlantic, linking SA with the tropical Indian
203 Ocean. An analysis of similar regression maps computed at different vertical levels reveals that the
204 circulation anomaly structures exhibit equivalent barotropic structures (not shown).

205

206 **3.2 SASS 10-30**

207

208 Regressions maps based on the SASS 10-30 Index were calculated between days -18 and
209 +18 and are discussed in this subsection. Regression maps for FOLR anomalies (Fig. 7) do not show
210 statistically significant convective anomalies at the equatorial Indian and Pacific oceans, in
211 opposition to the case of the SASS 30-90 (Fig. 3). It seems then that no significant MJO influence
212 can be identified on SASS 10-30 activity. This result disagrees with that obtained by Nogues-Paegle
213 et al. (2000), in which their mode 22, as well as their mode 40, were linked to tropical convective
214 activity. As it was discussed in section 2, the disagreement could be due to differences in the
215 methodologies applied to isolate the leading spatio-temporal modes of variability.

216 In general, spatially coherent significant FOLR anomalies are barely discernible outside of
217 SA in the SASS 10-30 cycle. However, a closer inspection reveals that both SICZ and SPCZ exhibit
218 some signs of activity (e.g.; at around day -12), though it is not possible to detect a clear life cycle
219 associated with these convergence zones. Between days -12 and -9, convection anomalies over SA
220 evolve towards a negative phase of SASS. That pattern weakens between days -9 and -6 and the
221 following shift in SASS phase is evident around days -6 and -3, with FOLR anomalies maximizing at
222 day 0. The SASS 10-30 related dipole also shows stationary features, with centers essentially
223 anchored throughout the whole evolution. The day-by-day evolution of the regressed values at
224 two locations representative of the SASS centers (Fig 8) reveals a certain lag in the opposite
225 relationship that both time series exhibit, that is not observed for SASS 30-90 (Fig. 4). In particular,
226 the negative peak of the subtropical center is reached at day -1 while the corresponding positive
227 peak of the SACZ center does it at day 0. This suggests that the timing of SASS 10-30 is dominated
228 by the SACZ center. In addition, the analysis of these time series confirms that the typical length of
229 the SASS 10-30 cycle is approximately 15 days.

230 Regression maps between the SASS 10-30 index and upper-level streamfunction anomalies
231 (Fig. 9) reveal at around day -15 the development of a teleconnection pattern along the South
232 Pacific Ocean, extended between 30 S and 40 S. As time evolves, circulation anomalies intensify
233 along the South Pacific, while they exhibit a weak eastward propagation. It can also be noted that
234 these wave trains exhibit a higher wavenumber than those identified for SASS 30-90 (Fig. 5). Over

235 SA, circulation anomalies become more stationary while northward meridional wave propagation
236 is discernible. At around day 0, the large-scale teleconnection pattern induces cyclonic
237 (anticyclonic) circulation anomalies at extratropical (tropical) SA, in association with a positive
238 phase of SASS 10-30 (Fig. 7). In addition, at approximately day +3, teleconnections develop from
239 SA eastward, crossing the South Atlantic and reaching the Indian Ocean. This wave train might be
240 induced by the SACZ enhancement observed between days -12 and -9 (Fig. 7). Grimm and Silva
241 Dias (1995), among others, confirmed through numerical experiments that such teleconnections
242 can develop. The wave structures emanating from SA northwards as well as eastwards have also
243 been identified by Nogues-Paegle et al. (2000) for mode 22, implying that they are robust signals
244 associated with SASS activity on shorter intraseasonal time scales. The vertical structure of these
245 wave trains are equivalent barotropic, as observed for the long intraseasonal time scales (not
246 shown). On the other hand, as opposed to what was observed for SASS 30-90 (Fig. 5), no tropical
247 wavenumber-1 structure is observed in the circulation anomalies associated with SASS 10-30
248 activity.

249

250 **4. SASS Energetics**

251 The previous analysis was complemented with an exploration of the energetics associated
252 with the evolution of both SASS 10-30 and SASS 30-90. Two different parameters describing the
253 eddy energy fluxes were considered in order to better understand the processes explaining the
254 development of the large-scale circulation anomalies associated with SASS evolution: the wave
255 activity fluxes (Plumb 1985) and the ageostrophic geopotential eddy fluxes (Orlanski and Katzfey
256 1991).

257 Wave activity flux (WAF) has been extensively used as diagnostic tool for the study of the
258 3D propagation of stationary waves. We considered the horizontal components of the fluxes as
259 defined by Schubert and Park (1991), for quasi-geostrophic stationary waves on a zonal mean flow:

$$F_{\lambda} = \frac{p}{2000a^2 \cos\varphi} \left[\frac{\partial \psi_r'^2}{\partial \lambda} - \psi_r' \frac{\partial^2 \psi_r'}{\partial \lambda^2} \right]$$

$$F_{\varphi} = \frac{p}{2000a^2} \left[\frac{\partial \psi_r'}{\partial \lambda} \frac{\partial \psi_r'}{\partial \varphi} - \psi_r' \frac{\partial^2 \psi_r'}{\partial \lambda \partial \varphi} \right]$$

260

261 where p stands for atmospheric pressure, φ for latitude, λ for longitude, a for the Earth's radius
 262 and ψ_r' are the temporal anomalies of the streamfunction previously regressed with the SASS
 263 index. WAF has proved to be useful in describing the source and propagation of Rossby waves
 264 (e.g.; Barlow et al. 2001; Brahmananda Rao et al. 2002). By design, WAF is parallel to wave group
 265 velocity and its divergence indicates the source regions for the perturbations. The meridional
 266 component, F_{φ} , depends on the momentum transport by the perturbations that is associated with
 267 the barotropic energy conversions. The zonal component, F_{λ} , is associated with the eddy
 268 horizontal structure. WAF were applied in the analysis of the perturbations presented in this work
 269 –even when they were strictly derived for stationary waves– under the assumption that the
 270 observed propagation speeds are very small.

271 The second methodology considered to describe eddy energy fluxes was the analysis of
 272 the ageostrophic geopotential eddy fluxes (e.g.; Chang and Orlanski 1994). Orlanski and Katzfey
 273 (1991) showed that when ageostrophic geopotential fluxes converge in a certain region, the
 274 creation of eddy kinetic energy is locally promoted. This mechanism frequently explains the
 275 generation of new perturbation centers downstream from the older centers, which radiate their
 276 energy through ageostrophic geopotential fluxes (e.g.; Orlanski and Katzfey 1991; Orlanski and
 277 Chang 1993; Chang 1993). In particular, Orlanski and Chang (1993) found that the downstream
 278 dispersion of wave energy via the ageostrophic geopotential fluxes was the triggering mechanism
 279 explaining downstream developing baroclinic waves over less baroclinic unstable regions.
 280 Furthermore, Chang and Orlanski (1994) showed that these energy fluxes are proportional to the
 281 group velocities of Rossby wave packets in baroclinic background flows.

282 This analysis is complemented with the evolution of the eddy kinetic energy (K_e), which
 283 was computed from the regressed values of both zonal and meridional winds at 200 hPa, onto the
 284 SASS indexes:

285

$$K_e = \frac{1}{2} [u_r'^2 + v_r'^2]$$

286

287 where ' represents temporal anomalies and the subindex r implies that the regressed variables
288 are considered. The ageostrophic geopotential fluxes play a role on the equation that describes
289 the evolution of the eddy kinetic energy and therefore, a combined analysis of these parameters
290 can help identify the processes that explain the observed evolution of circulation anomalies.

291

292 **3.4.1 SASS 30-90**

293 The WAF evolution associated with SASS 30-90 is presented in left column of Figure 11.
294 Starting around day -25, at the beginning stages of the SASS negative phase, a divergence in the
295 WAF is observed over New Zealand. During the following days, fluxes organize, evidencing an arch-
296 shaped structure along the South Pacific. Between days -25 and -20 the first signs of inter-
297 hemispheric energy propagation are observed in the tropical eastern Pacific and tropical western
298 Atlantic, coinciding with the equatorial mean 'westerly ducts' (not shown). By day -15, when the
299 SASS negative phase is dissipating, it is possible to notice how the SACZ starts acting as a new wave
300 source region, with fluxes that radiate towards the South Atlantic and reaching the Indian Ocean.
301 Between days -15 and 0, fluxes are considerably strong over eastern SA, in association with the
302 development of the SASS positive phase. Between days +5 and +10, the fluxes over SASS region
303 weaken, coinciding with a new phase shift of the SASS. Furthermore, by day +10 a new WAF
304 divergence region is observed over Australia and the fluxes progressively reorganize across the
305 South Pacific, which is consistent with what was observed in Figure 4.

306 The evolution of the ageostrophic geopotential fluxes at 200 hPa was also analyzed for
307 SASS 30-90 (Fig. 11b). Fluxes are significant in isolated and discontinuous regions, located between
308 Ke centers (contours) and generally radiating downstream. Consistently with Figure 11a, the first
309 days of the evolution reveal energy radiating from a convectively active region northeast of
310 Australia (Fig. 3) and some inter-hemispheric propagation, particularly over the tropical Pacific is
311 discernible. Between days -15 and -10, significant ageostrophic fluxes are observed over SESA,
312 coinciding with a shift from the negative to the positive SASS phase. Subsequently, the SASS region
313 starts acting as a wave source, with energy radiating towards the South Atlantic. Between days -
314 10 and -5, the alternating areas with fluxes delimit an arch-shaped structure connecting the
315 vicinity of New Zealand with SA, in agreement with the circulation anomalies in Fig. 5. The

316 weakening of some centers, like the one located to the SE of Australia, is accompanied by the
317 divergences of the ageostrophic flows. Between days +5 and +10, fluxes over the SASS region
318 weaken, consistently with another phase shift.

319

320 **4.2 SASS 10-30**

321 WAF evolution for SASS 10-30 (Fig. 12a) presents the first significant signals between days
322 -15 and -12, associated with zonally oriented fluxes starting at around 180° W and south of 40° S,
323 along the southern branch of the westerly jet. Starting from day -9, when negative SASS phase
324 settles, WAF intensifies over SA with a very strong SW-NE orientation.. An arch-shaped wave flux
325 structure connecting the region to the SE of New Zealand with SA develops between days -6 and
326 day +6. In particular, between days -3 and +3, a positive SASS phase progresses, while alternate
327 centers of flux divergence and convergence propagate northeastwards over SA. Also, between
328 days 0 and +3 part of the fluxes radiate towards the South Atlantic and converge over southern
329 Africa. By days +3 and +6 large fluxes are observed along the Indian Ocean, and converging in the
330 vicinity of Australia.

331 Figure 12b presents the evolution of the ageostrophic geopotential fluxes (vectors) and of
332 K_e (contours). On day -15, the first significant fluxes are observed over the SW Pacific, in the
333 proximities of New Zealand. Fluxes suggest that the observed wave trains originate from the
334 westerlies channels near the date line. This feature allows to speculate that their generation is
335 associated with changes in the divergence within the westerly jet (Weickmann 1983; Weickmann
336 et al. 1985; Berbery and Nogues-Paegle 1992). Another notorious feature is the absence of K_e
337 centers in the tropical band, near Africa and the Indian Ocean, that was previously linked for the
338 30-90 activity band with the tropical convective anomalies (Fig. 11a). From day -12, significant
339 fluxes are observed in the proximities of southwestern SA, leading to the development of a
340 negative SASS phase. They start being zonally-oriented but from day -9 onwards they acquire a
341 SW-NE orientation and intensify notoriously. By that time, cross-equatorial propagation over the
342 tropical Atlantic is discernible. Between days -3 and +3, a strong flux divergence establishes over
343 SESA simultaneously with a shift to the positive SASS phase. After day 0, as for WAF, the
344 connection between the SASS region and the South Atlantic is evident. However, unlike what was
345 found for SASS 30-90, no arch-shaped structure in the propagation over the South Pacific is

346 observed by that time. The fluxes tend to be very weak in the western portion of the basin and to
347 be zonally oriented in the south and southeast portions.

348

349 **5. Summary and Discussion**

350

351 This work explored the activity of the leading pattern of precipitation intraseasonal
352 variability over SA –the SASS pattern– in its main activity bands: 30-90 days and 10-30 days. Two
353 SASS patterns and their respective time series were obtained by performing two separate EOF
354 analyses of the corresponding filtered OLR anomalies. It was found that for both bands of
355 variability SASS is related to a dipole-like structure with OLR anomalies of opposite signs over the
356 SESA and SACZ regions. For each SASS the large-scale features associated with the SASS activity
357 were analyzed.

358 SASS activity in the 30-90 day band is characterized by a tropical dipole in convection that
359 propagates to the east across the Indian and western Pacific Oceans. The associated circulation
360 anomalies are characterized by a strong eastward propagating wavenumber-1 structure in the
361 tropics. This observed evolution of both tropical convection and circulation anomalies is consistent
362 with the life cycle of the MJO. In addition, the activity of the SASS 30-90 seems to be linked with
363 tropical convection through Rossby-like wave trains with arch-shaped trajectories across the
364 Southern Pacific ocean. The observed wave trains are equivalent barotropic and quasi-stationary.

365 On the other hand, the activity in the 10-30 day band does not seem to be connected with
366 variations in the tropical convection. The evolution of the upper-level streamfunction regressions
367 for the SASS 10-30 showed Rossby-like wave trains, as in the case of the 30-90 band, but that
368 appear to originate in the subtropics, and not connected to significant convective anomalies. In
369 addition, these waves showed larger propagation speeds than in the 30-90 case, though still weak.
370 The fact that there are no clear subtropical convective sources for the observed wave trains does
371 not necessarily imply that this mechanism is not present in this activity band. It might be the case
372 that no clear source region can be detected due to the averaging procedure involved in the
373 regressions calculation, combining cases with different source regions or triggering mechanisms

374 (Kiladis, personal communication). In addition, this higher frequency intraseasonal variability
375 might be the result of modulations of synoptic-scale perturbations or of multi-scale interactions.

376 The study of the evolution of the eddy kinetic energy, along with the wave activity fluxes
377 and the ageostrophic geopotential fluxes allowed to confirm that certain features of the observed
378 wave activity, such as the presence of inter-hemispheric propagation and the arch-shaped
379 patterns, can be explained by mechanisms such as barotropic energy conversion and downstream
380 development of anomalous K_e centers.

381 In summary, this analysis allows to conclude that the SASS activity in the 30-90 band is
382 strongly influenced by the MJO, through the excitation of Rossby-like wave trains in the tropics. In
383 contrast, tropical convective activity does not seem to be involved in the triggering of SASS activity
384 in the 10-30 day band. The latter seems to be linked to similar wave trains but that have
385 subtropical sources, and could be related to changes in the properties of the westerly jet. A case
386 study approach is proposed as an alternative method for exploring the large-scale features of this
387 activity band, which could also inspire numerical simulations to complement the understanding of
388 the dynamical mechanisms involved.

389 Finally, the evolutions of the OLR and streamfunction regressions suggest that there might
390 be a significant interaction between the subtropical convergence zones (SPCZ, SACZ and SICZ) on
391 intraseasonal timescales, as previously suggested by other authors (e.g.; Cook et al. 2004). Future
392 studies will focus on better understanding these interactions as well as exploring how the large-
393 scale features associated with both activity bands interfere constructively or destructively to
394 determine the local SASS conditions.

395

396 **5 Acknowledgements**

397 This research was supported by UBACyT 20020100100434, and ANPCyT/PICT-2010-2110.

398

399 **6 References**

400 Barlow M, Nigam S, Berbery EH (2001) ENSO, Pacific decadal variability, and U.S. summertime

401 precipitation, drought, and streamflow. *J Climate*, 14: 2105-2128.

402

403 Berbery EH, Nogues-Paegle J, Horel JD (1992) Wavelike Southern Hemisphere extratropical
404 teleconnections. *J Atmos Sci*, 49:155-177.

405

406 Brahmananda Rao V, Chapa SR, Fernandez JPR, Franchito SH (2002) A diagnosis of rainfall over
407 South America during the 1997/98 El Niño event. Part II: Roles of water vapor transport and
408 stationary waves. *J Climate*, 15:513–522.

409

410 Bjornsson H, Venegas SA (1997) A manual for EOF and SVD analyses of climate data. CCGCR Rep.
411 97-1, McGill University, Montreal, QC, Canada, 52 pp.

412

413 Carvalho LMV, Jones C, Liebmann B (2004) The South Atlantic convergence zone: Intensity, form,
414 persistence, and relationships with intraseasonal to interannual activity and extreme rainfall. *J*
415 *Climate*, 17: 88-108.

416

417 Casarin DP, Kousky VE (1986) Anomalias de precipitação no sul do Brasil e variações na circulação
418 atmosférica. *Rev Bras Meteorol*, 1, 83-90.

419

420 Cavalcanti IFA, Castro CC (2003) Southern Hemisphere atmospheric low frequency variability in a
421 GCM climate simulation. VII international Conference on Southern Hemisphere Meteorology and
422 Oceanography, 24-28 March 2003, Wellington, New Zealand.

423 Cerne B, Vera C, Liebmann B (2007) The nature of a heat wave in eastern Argentina occurring
424 during SALLJEX. *Mon Wea Rev*, 135:1165-1174.

425 Cerne B, Vera C (2011) Influence of the intraseasonal variability on heat waves in subtropical South
426 America. *Clim Dyn*, 36: 2265-2277.

427 Chang EKM (1993) Downstream Development of Baroclinic Waves as Inferred from Regression
428 Analysis. *J Atmos Sci*, 50:2038-2053.

429 Chang EKM, Orlanski I (1994) On Energy Flux and Group Velocity of Waves in Baroclinic Flows. *J*
430 *Atmos Sci*, 51:3823-3828.

431 Cook KH (2000) The South Indian convergence zone and interannual rainfall variability over
432 southern Africa. *J Climate*, 13:3789-3804.
433

434 Cook KH, Hsieh J, Hagos S (2004) The Africa–South America intercontinental teleconnection. *J*
435 *Climate*, 17:2851-2865.
436

437 Cunningham CC, Cavalcanti IFA (2006) Intraseasonal modes of variability affecting the South
438 Atlantic Convergence Zone. *Int J Climatol*. doi: 10.1002/joc.1309.
439

440 Diaz A, Aceituno P (2003) Atmospheric circulation anomalies during episodes of enhanced and
441 reduced convective cloudiness over Uruguay. *J Climate*, 16:3171-3185.
442

443 Duchon CE (1979) Lanczos Filtering in One and Two Dimensions. *J Appl Meteor*, 18:1016-1022.
444

445 Ferranti L, Palmer TN, Molteni F, Klinker E (1990) Tropical-Extratropical Interaction Associated with
446 the 30–60 Day Oscillation and Its Impact on Medium and Extended Range Prediction. *J Atmos Sci*,
447 47: 2177-2199.

448 Grimm AM, Silva Dias PL (1995) Analysis of tropical–extratropical interactions with influence
449 functions of a barotropic model. *J Atmos Sci*, 52:3538-3555.
450

451 Gonzalez PLM, Vera CS, Liebmann B, Kiladis G (2008) Intraseasonal variability in subtropical South
452 America as depicted by precipitation data. *Clim Dyn*, 30:727-744.

453 Hendon H, Salby M (1994) The life cycle of the Madden–Julian oscillation. *J Atmos Sci*, 51: 2225-
454 2237.
455

456 Jones C, Schemm J-K E (2000) The influence of intraseasonal variations on medium-range weather
457 forecasts over South America. *Mon Wea Rev*, 128:486-494.

458 Kalnay E, Mo KC, Paegle J (1986) Large-amplitude, short-scale stationary Rossby waves in the
459 southern hemisphere: Observations and mechanistic experiments to determine their origin. *J*
460 *Atmos Sci*, 43:252-275.
461

462 Kalnay E et al. (1996) The NCEP/NCAR 40-Year Reanalysis Project. Bull Amer Meteor Soc, 77:437-
463 471.
464

465 Li XL, Le Treut H (1999) Transient behavior of the meridional moisture transport across South
466 America and its relation to atmospheric circulation patterns. Geophys Res Lett, 26, 10, 1409-1412.

467 Liebmann B, Smith CA (1996) Description of a Complete (Interpolated) Outgoing Longwave
468 Radiation Dataset. Bull Am Meteor Soc, 77:1275-1277.
469

470 Liebmann B, Kiladis GN, Marengo JA, Ambrizzi T, Glick JD (1999) Submonthly convective variability
471 over South America and the South Atlantic convergence zone. J Climate, 12:1877-1891.
472

473 Liebmann, B, Kiladis GN, Vera CS, Saulo AC, Carvalho LMV (2004) Subseasonal variations of rainfall
474 in South America in the vicinity of the low-level jet east of the Andes and comparison to those in
475 the South Atlantic convergence zone. J Climate, 17:3829-3842.
476

477 Lin JL et al. (2006) Tropical intraseasonal variability in 14 IPCC AR4 climate models. Part I:
478 Convective signals. J Climate, 19:2665-2690.

479 Mo KC, Higgins RW (1998) The Pacific–South American Modes and Tropical Convection during the
480 Southern Hemisphere Winter. Mon Wea Rev, 126:1581-1596.

481 Mo KC, Nogues-Paegle J (2001) The Pacific-South American modes and their downstream effects.
482 Int. J of Climatol, 21:1211-1229.

483 Nogues-Paegle J, Mo KC (1997) Alternating wet and dry conditions over South America during
484 summer. Mon Wea Rev, 125:279-291.
485

486 Nogues-Paegle J, Byerle LA, Mo KC (2000) Intraseasonal modulation of South American summer
487 precipitation. Mon Wea Rev, 128: 837-850.
488

489 Orlanski I, Katzfey J (1991) The life cycle of a cyclone wave in the Southern Hemisphere. Part I:
490 Eddy energy budget. J Atmos Sci, 48:1972-1998.
491

492 Orlanski I, Chang EKM (1993) Ageostrophic geopotential fluxes in downstream and upstream
493 development of baroclinic waves. *J Atmos Sci*, 50:212-225.
494

495 Plumb RA (1985) On the three-dimensional propagation of stationary waves. *J Atmos Sci*, 42:217-
496 229.
497

498 Sardeshmukh PD, Hoskins BJ (1988) The Generation of Global Rotational Flow by Steady Idealized
499 Tropical Divergence. *J Atmos Sci*, 45:1228-1251.

500 Schubert SD, Park C-K (1991) Low-frequency intraseasonal tropical–extratropical interactions. *J*
501 *Atmos Sci*, 48:629-650.
502

503 Slingo JM et al. (1996) Intraseasonal oscillations in 15 atmospheric general circulation models:
504 Results from an AMIP diagnostic subproject. *Clim Dyn* 12: 325-357.

505 Vincent DG (1994) The south pacific convergence zone (SPCZ): a review. *Mon Weath Rev*,
506 122:1949-1970.

507 Waliser DE, Lau KM, Stern WF, Jones C (2003) Potential predictability and the Madden-Julian
508 Oscillation. *Bull Am Meteor Soc*, 84: 33-50.

509 Weickmann KM (1983) Intraseasonal circulation and outgoing longwave radiation modes during
510 Northern Hemisphere winter. *Mon Wea Rev*, 111:1838-1858.
511

512 Weickmann KM, Lussky GR, Kutzbach JE (1985) Intraseasonal (30–60 day) fluctuations of outgoing
513 longwave radiation and 250 mb streamfunction during northern winter. *Mon Wea Rev*, 113:941-
514 961.
515

516

517

518

519 **Figure Captions**

520

521 **Figure 1:** SASS pattern for the band: (a) 30-90 days, (b) 10-30 days, defined as the first EOF of
522 filtered summer NOAA OLR for the period 1979-2007. The number between parenthesis indicates
523 the amount of total FOLR variance explained by the pattern.

524 **Figure 2:** Power spectra of the SASS Index for the 10-30-days band (thick blue curve) and the 30-
525 90-days band (thick red curve). The thin lines represent the null continuum, with respect to a red
526 noise spectrum, and the 5% and 95% confidence levels.

527 **Figure 3:** Lagged regressions between the SASS 30-90 index and FOLR 10-90. Negative days
528 indicate that FOLR is leading the evolution. Shaded colors are statistically significant at the 95%
529 confidence level, according to a Student *t*-test. Contour interval is 1 W/m² and negative OLR
530 anomalies (enhanced convection) is depicted in green.

531 **Figure 4:** Evolution of lagged regressions between the SASS 30-90 index and FOLR 10-90 in the
532 centers of the dipole: 30° S 60° W (SESA center, green curve, full circles) and 10° S 50° W (SACZ
533 center, black curve, open circles).

534 **Figure 5:** Lagged regressions between the SASS 30-90 index and zonal anomalies of
535 streamfunction at $\sigma = 0.2101$. Negative days indicate that streamfunction is leading the
536 evolution. Shaded colors are statistically significant at the 95% confidence level, according to a
537 Student *t*-test. Contour interval is $5 \times 10^5 \text{ m}^2/\text{s}$.

538 **Figure 6:** Hovmöller diagram of lagged regressions between the SASS 30-90 index and zonal
539 anomalies of streamfunction at $\sigma = 0.2101$ for the average of latitudes in the 20° S – Equator
540 band. Shaded colors are statistically significant at the 95% confidence level, according to a Student
541 *t*-test. Contour interval is $0.5 \times 10^6 \text{ m}^2/\text{s}$.

542 **Figure 7:** As Figure 3 but for the SASS 10-30.

543 **Figure 8:** As Figure 4 but for the SASS 10-30.

544 **Figure 9:** As Figure 5 but for the SASS 10-30.

545 **Figure 10:** Hovmöller diagram of lagged regressions between the SASS 30-90 index and zonal
546 anomalies of streamfunction at $\sigma = 0.2101$ for the average of latitudes in the 60° S - 40° S band.
547 Shaded colors are statistically significant at the 95% confidence level, according to a Student
548 *t*-test. Contour interval is $0.5 \times 10^6 \text{ m}^2/\text{s}$.

549 **Figure 11:** Energetics of the 30-90 day band. The left panel presents the evolution of the wave
550 activity fluxes obtained from the regressions with streamfunction at $\sigma = 0.2101$. The scale for the
551 vectors is in the bottom right corner and the units are m^2/s^2 . The shading describes the
552 divergence of the fluxes and the units are m/s^2 . The right panel presents the ageostrophic
553 geopotential fluxes obtained from the regressions with wind and geopotential heights at 200 hPa.
554 The units are m^2/s . The contours present the evolution of the eddy kinetic energy constructed
555 using the regressions between wind anomalies at 200 hPa and the SASS 30-90 Index. The contour
556 interval is $0.5 \text{ m}^2/\text{s}^2$. In all the panels the plotted values are statistically significant at the 95%
557 level.

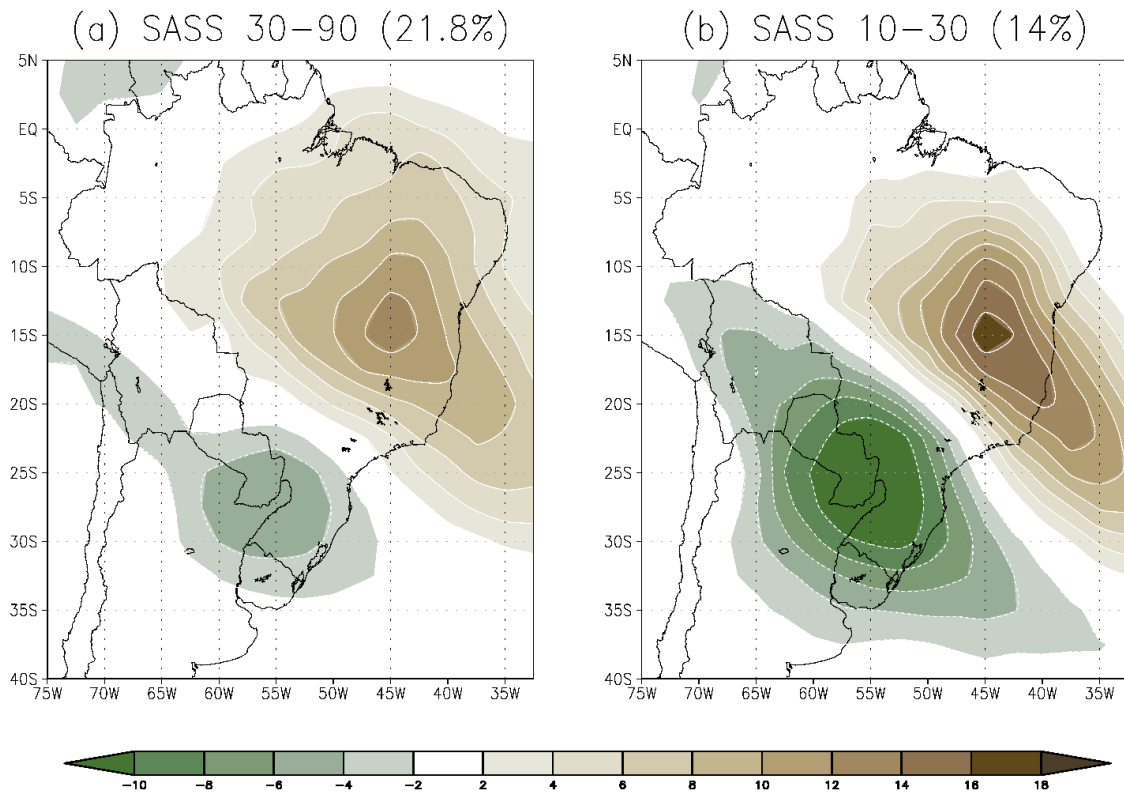
558

559 **Figure 12:** Same as Figure 11 but for the 10-30 day band.

560

561 **Figures**

562 Figure 1



563

564

565

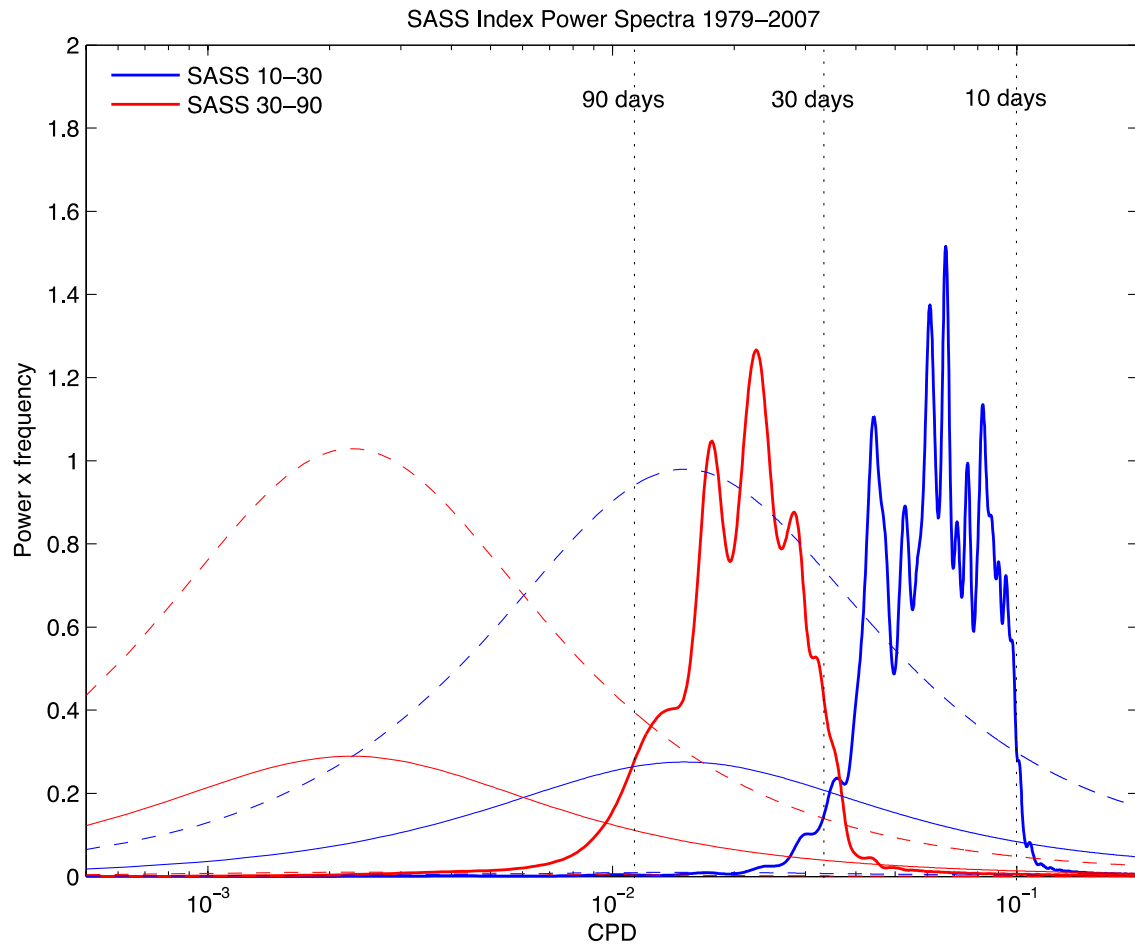
566

567

568

569

570 Figure 2



571

572

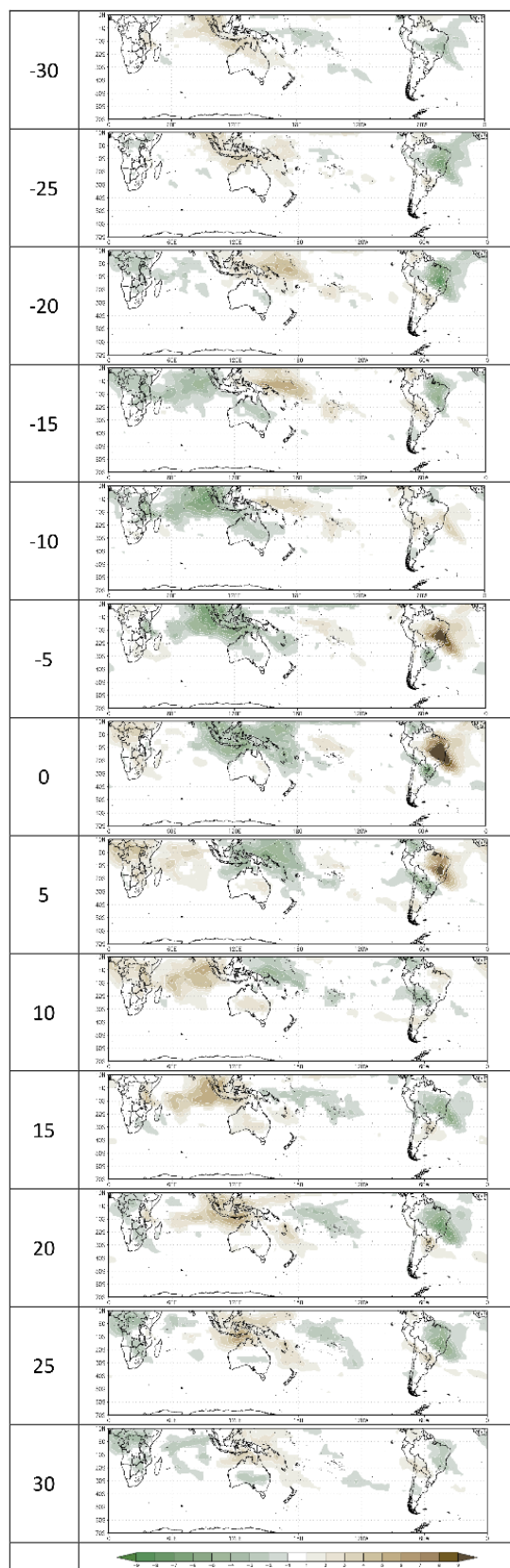
573

574

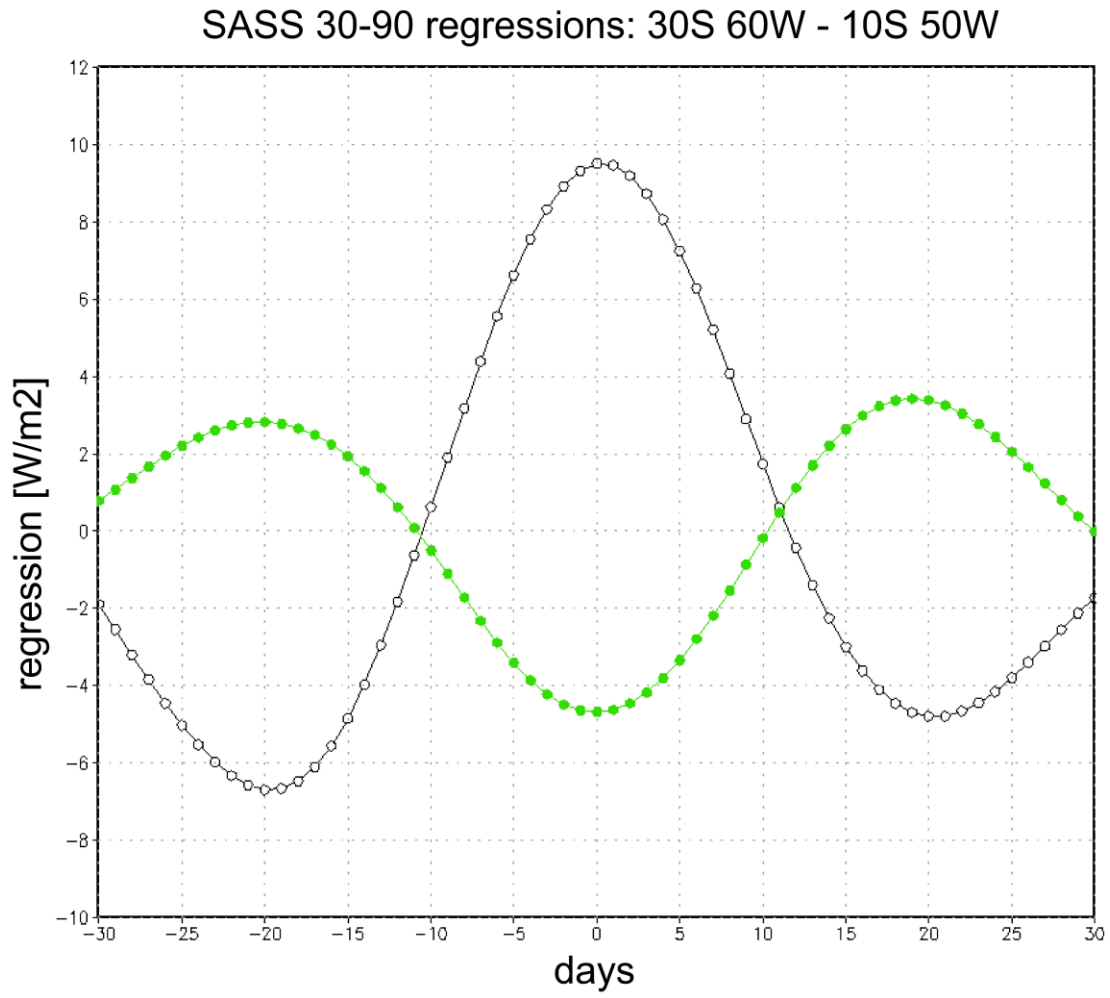
575

576

577



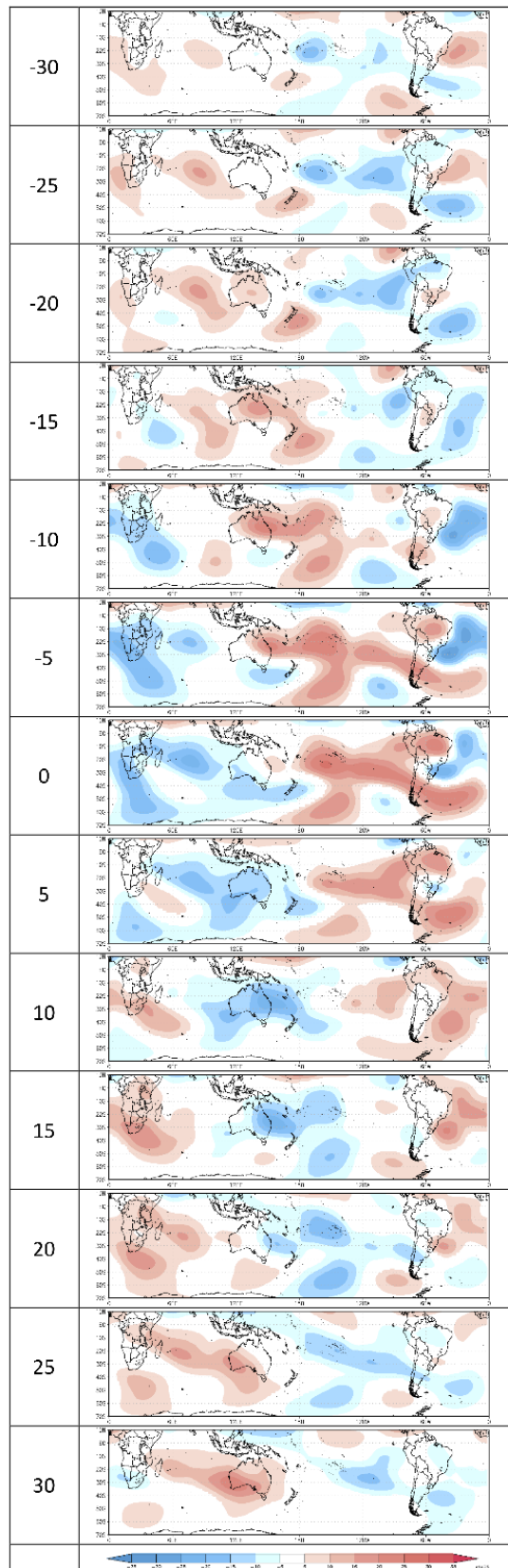
580 Figure 4



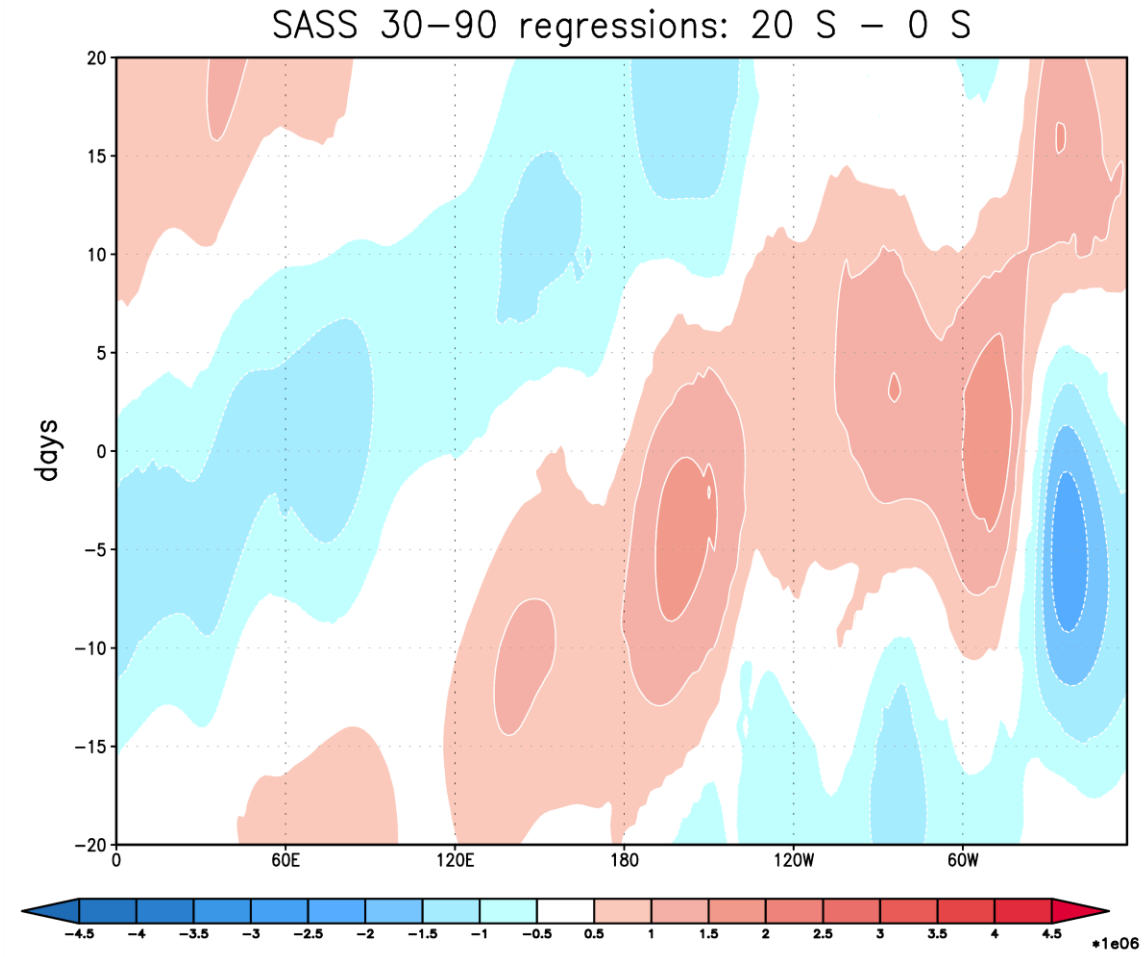
581

582

583



586 Figure 6



587

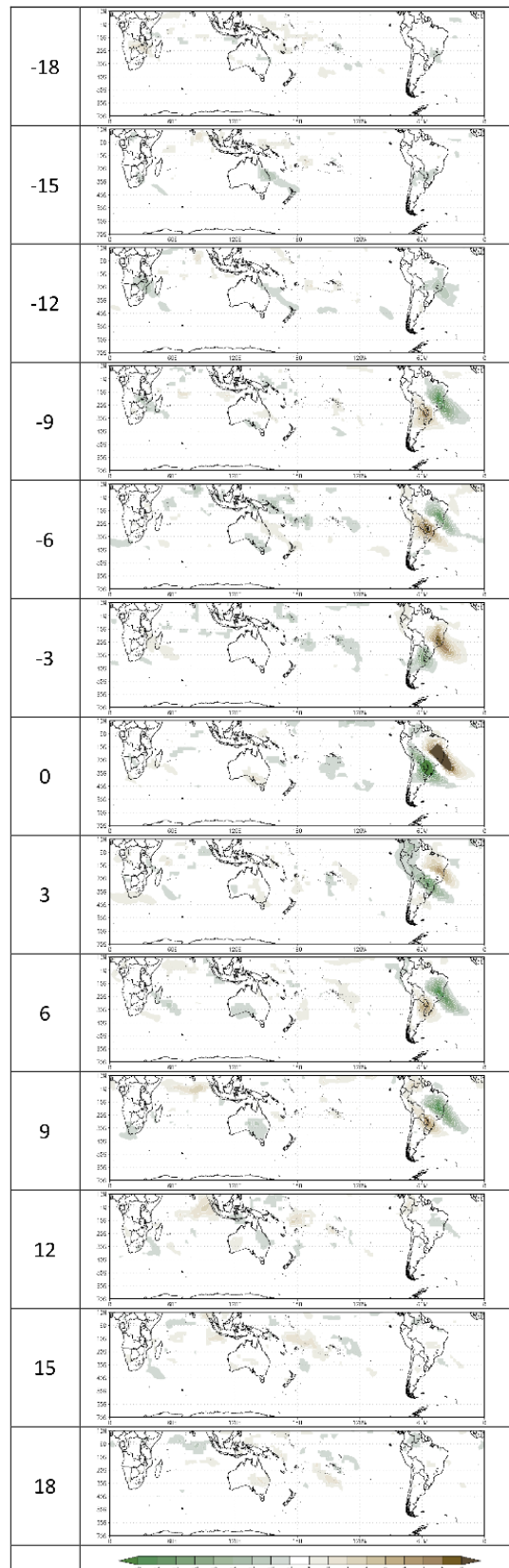
588

589

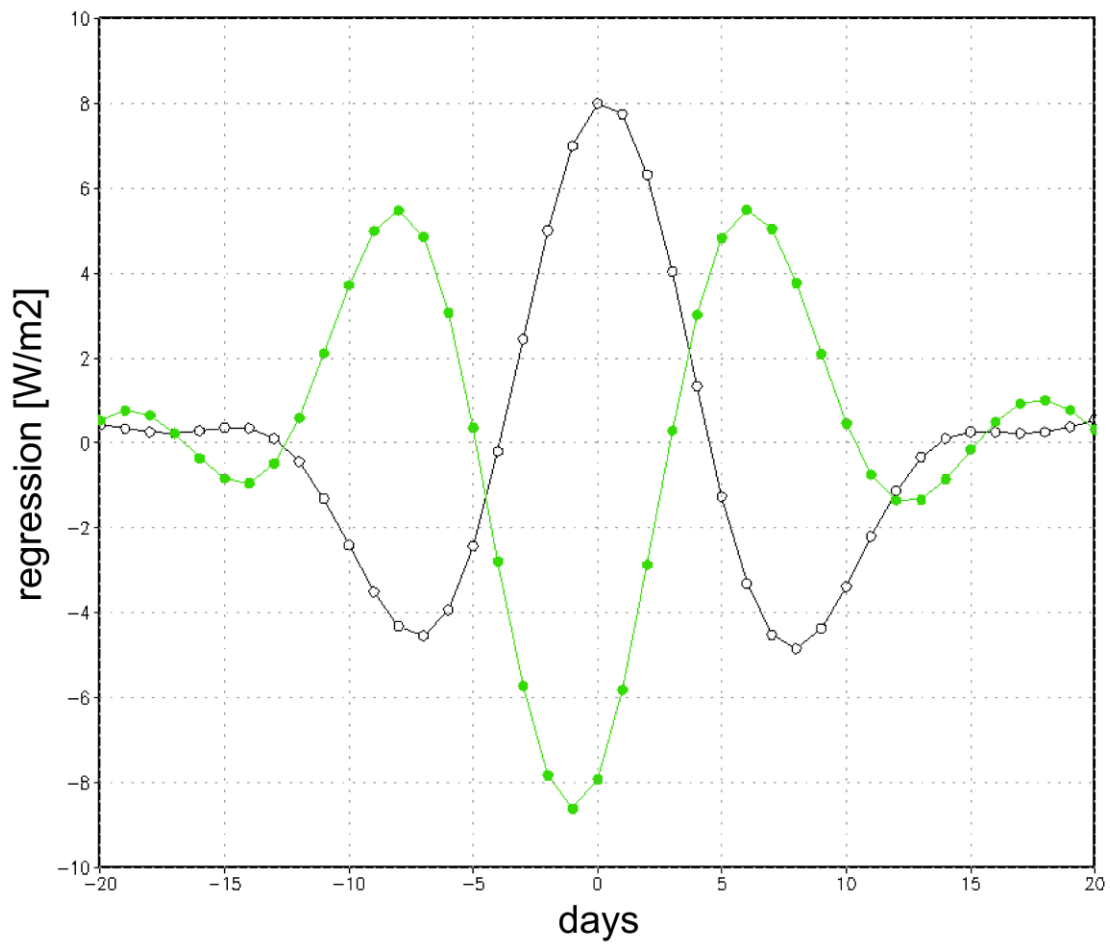
590

591 Figure 7

592



SASS 10-30 regressions: 30S 60W - 10S 50W



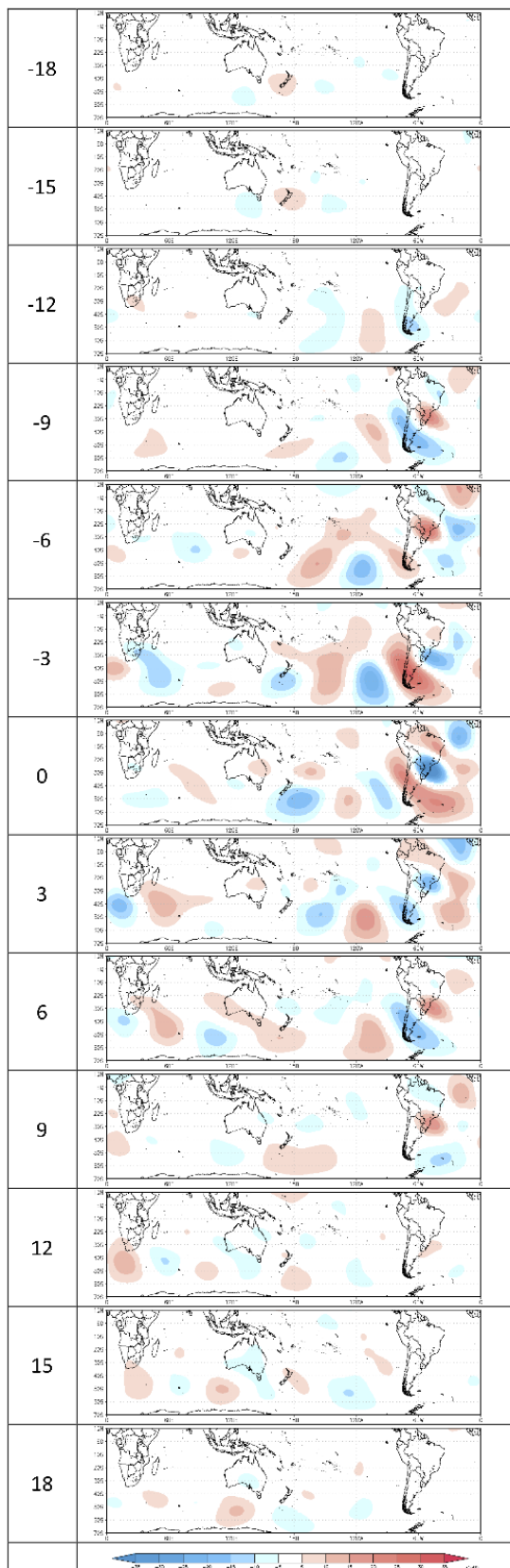
594

595

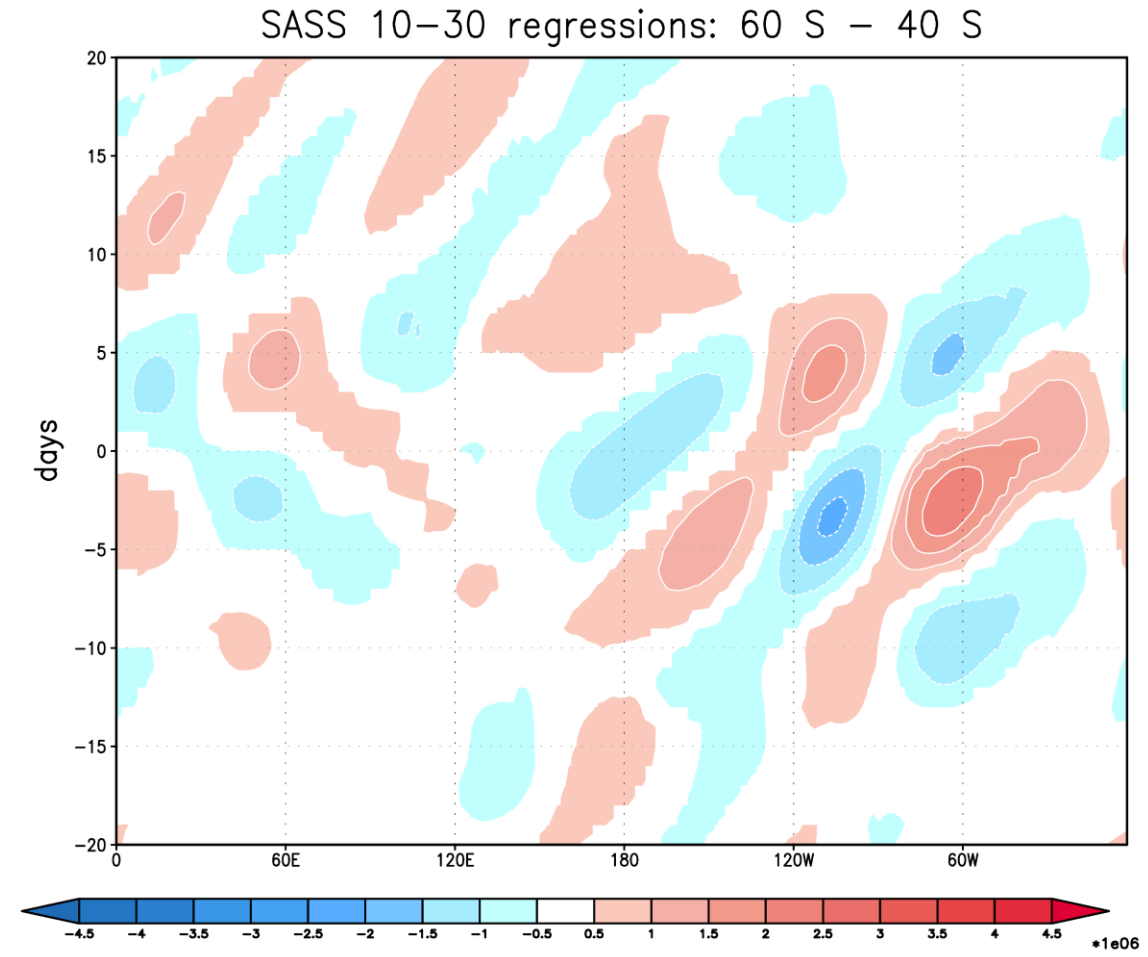
596

597

598



601 Figure 10



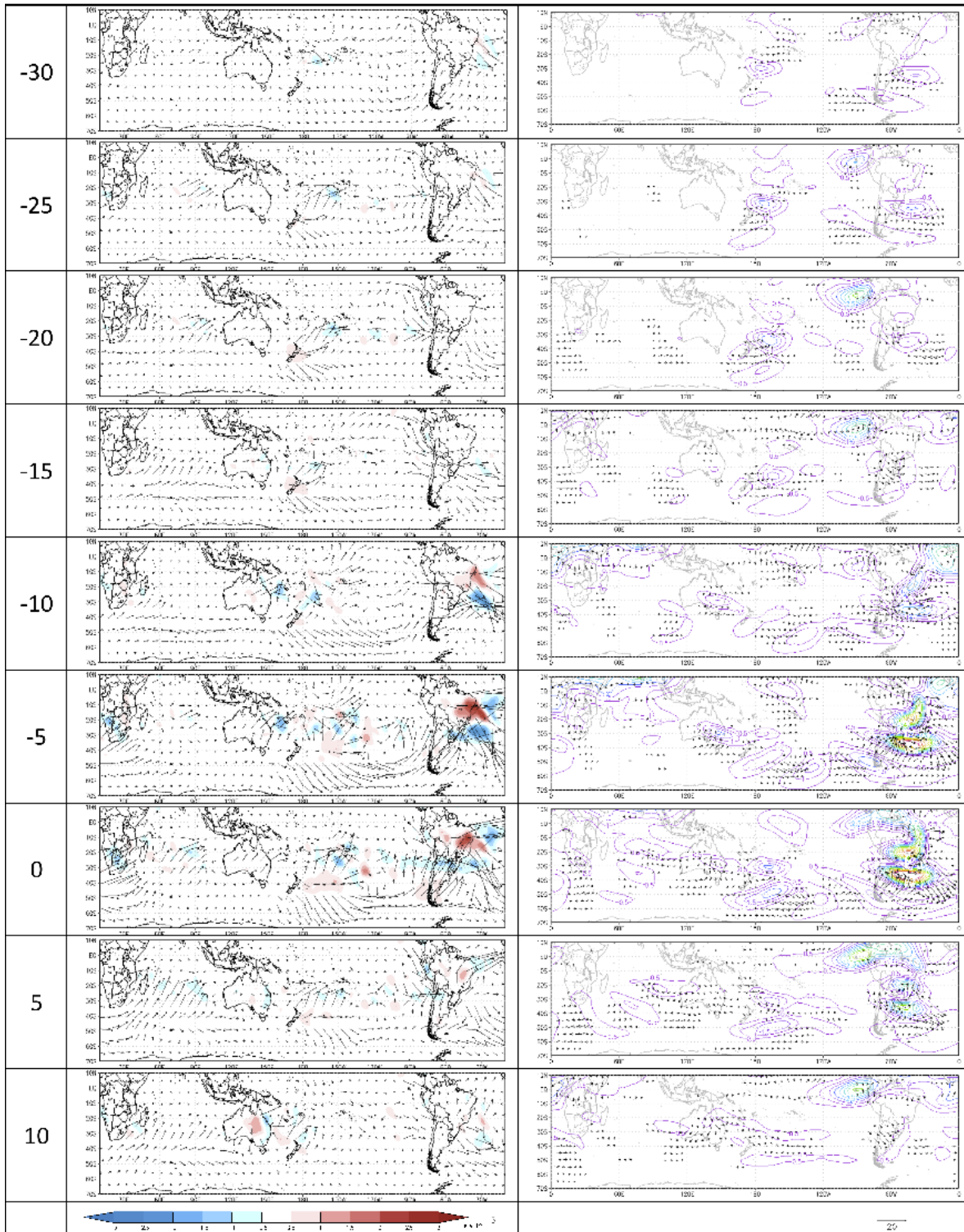
602

603

604

605

606 Figure 11

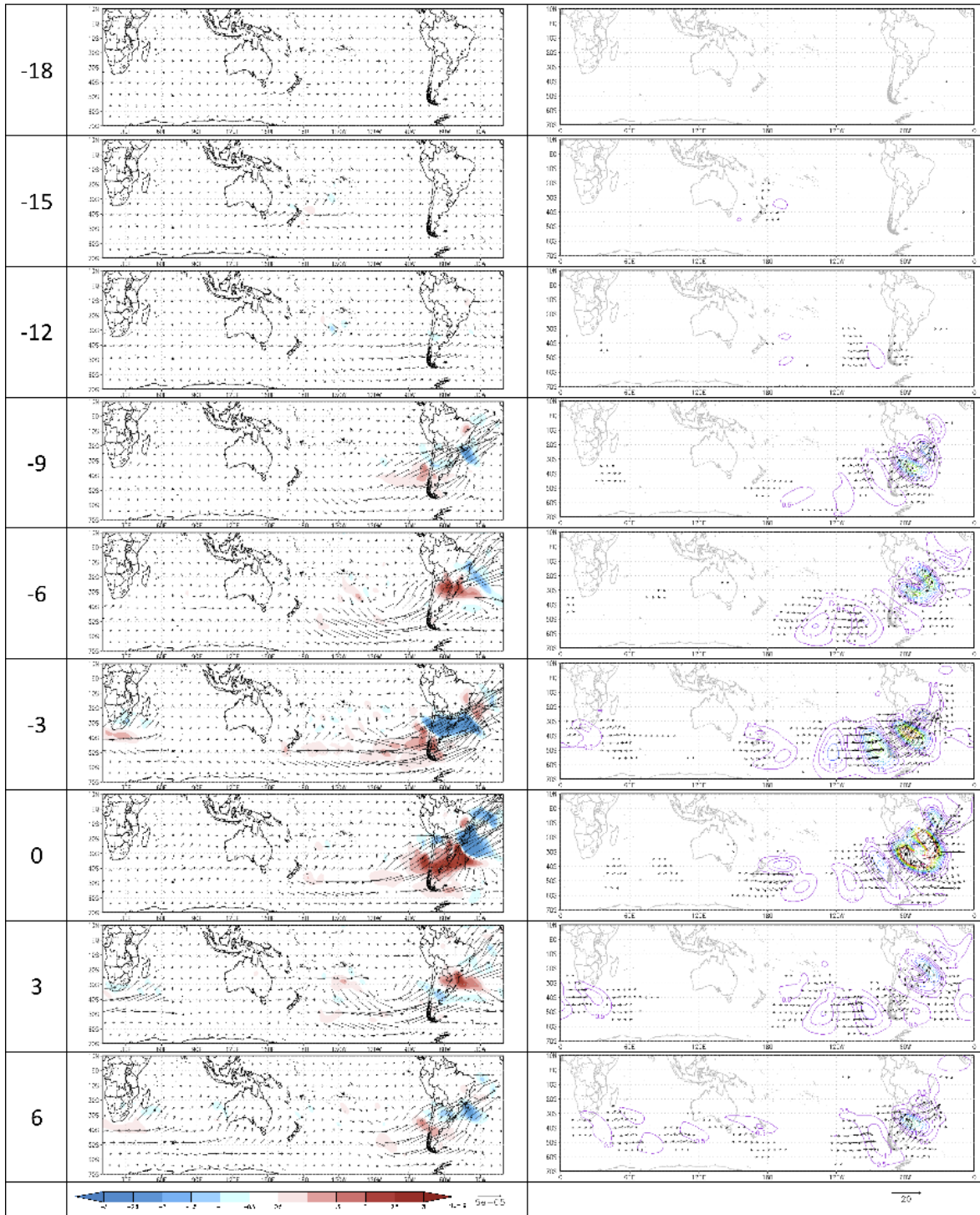


607

608

609

610 Figure 12



611